International Journal of Heat and Mass Transfer 146 (2020) 118802

Contents lists available at ScienceDirect

International Journal of Heat and Mass Transfer

journal homepage: www.elsevier.com/locate/ijhmt

Theoretical Leidenfrost point (LFP) model for sessile droplet

Chang Cai [a,b], Issam Mudawar [b,*], Hong Liu [a], Chao Si [a]

[a] Key Laboratory of Ocean Energy Utilization and Energy Conservation of Ministry of Education, School of Energy and Power Engineering, Dalian University of Technology, Dalian 116024, PR China

[b] Purdue University Boiling and Two-Phase Flow Laboratory (PU-BTPFL), School of Mechanical Engineering, 585 Purdue Mall, West Lafayette, IN 47907, USA

ARTICLE INFO

Article history:
Received 9 June 2019
Received in revised form 2 August 2019
Accepted 27 September 2019
Available online 16 October 2019

Keywords:
Leidenfrost point (LFP)
Sessile droplets
Droplet evaporation
Surface roughness

ABSTRACT

In the present paper, a theoretical investigation is undertaken in pursuit of a new mechanistically based Leidenfrost point (LFP) model for a sessile droplet. The model consists of sub-models describing temporal variations of droplet size and shape, and thickness of the vapor layer separating the droplet from the heating surface during the evaporation process. Starting from the film boiling regime, it is shown that decreasing surface temperature causes monotonic thinning of the vapor layer. The primary hypothesis of the model is that as Leidenfrost temperature is reached, the vapor layer becomes sufficiently thin to enable surface roughness protrusions to breach the droplet underside. It is shown that, because of the stochastic nature of surface roughness, an appropriate statistical parameter of surface height must be determined for comparison with the vapor layer thickness. Using surface profiles measured by the authors along with those obtained from prior studies, it is shown how this statistical parameter may be related to other commonly available parameters. Overall, the model shows good accuracy in predicting temporal records of droplet size and shape, and vapor layer thickness for different liquids and surface temperatures. Combined with the statistical surface height parameter, the model shows very good accuracy in predicting the Leidenfrost temperature, evidenced by a mean absolute error of 7.77%.

1. Introduction

1.1. Critical modeling needs in boiling heat transfer

Despite the recent proliferation of studies on two-phase flow and heat transfer, those providing mechanistic depiction of dominant mechanisms and, perhaps more importantly, theoretical predictive tools for parameters that are essential to assessment of the performance of industrial systems adopting two-phase heat transfer as well as system design, are quite sparse. In a recent study [1], key phenomena demanding such tools were identified, which include critical heat flux (CHF) and the Leidenfrost Point (LFP). The present study is focused entirely on the latter.

As discussed in the next subsection, the LFP is especially important in the spray cooling process employed in metal alloy heat-treating operations. Generally speaking, spray cooling is a prime contender for a variety of applications involving removal of concentrated heat loads, competing with pool boiling (also bath quenching), macro- and micro-channel flow boiling, and jet impingement [2]. While each of these cooling schemes provides multiple advantages, there are also important challenges. For example, pool boiling, while being the simplest and least expensive, is incapable of tackling high heat flux situations [3]. Flow boiling in macro- and micro-channels is known to yield very high heat transfer coefficients using very compact and lightweight hardware, but poses the challenges of strong axial variations in surface temperature and high pressure drop. Jet impingement, which, like spray cooling, is also popular for quenching of metal alloys, can yield very high heat transfer coefficients, albeit at the expense of high coolant flow rate and large spatial variations in surface temperature (which often demands use of multiple jets [4]). Two key advantages of spray cooling are ability to reduce coolant flow rate requirements and far better surface temperature uniformity than possible with the competing schemes [5]. With sprays, this temperature uniformity is derived from breakup of liquid into fine droplets having large surface area to volume ratio, and which impact the surface in a fairly diffuse manner (as opposed to the highly concentrated jet impingement).

However, there is far less technical knowhow on spray cooling that on its competitors, given the sensitivity of spray cooling to several complex and interrelated processes, including droplet breakup at the outlet of the spray nozzle, multiple trajectories of droplet streams, and, most importantly, droplet impact on the surface [2,6].

* Corresponding author.
E-mail address: mudawar@ecn.purdue.edu (I. Mudawar).
URL: https://engineering.purdue.edu/BTPFL (I. Mudawar).

https://doi.org/10.1016/j.ijheatmasstransfer.2019.118802
0017-9310/

Nomenclature

A	area
A_F	frontal area of droplet
c	concentration
D	mass diffusion coefficient; equivalent droplet diameter
D_0	initial droplet diameter
f_1, f_2	functions defined in Eqs. (18a) and (18b), respectively
g	gravity
h_{fg}	latent heat of vaporization
k	thermal conductivity
L	surface profile sampling length
l	capillary length
M	molar mass [kg/mol]
m	mass
n	number of surface profile sampling points
P	pressure
P_0	liquid pressure at $r = 0$
p_i	local peak height of surface profile
R_s	distance from coordinate center to droplet surface
R_a	arithmetic mean surface roughness
R_g	gas constant [kJ/(kg·mol)]
R_{max}	maximum radius of droplet (defined in Fig. 3)
R_{neck}	neck radius of droplet (defined in Fig. 3)
R_{patch}	patch radius of droplet (defined in Fig. 3)
R_q	root mean square of surface roughness
R_z	average height of surface roughness
r	radial coordinate along heating surface (defined in Fig. 3)
r_s	spherical coordinate (defined in Fig. 3)
s	arc length
T	temperature
T_{sat}	saturation temperature
T_w	wall (heating surface) temperature
u	vapor layer velocity in r direction (defined in Fig. 3)
V	volume
v	vapor production rate per unit area (defined in Fig. 3)
v_i	local valley depth in surface profile ($v_i < 0$)
w	vapor velocity in z direction
x	surface profile measurement direction
y_i	local height of surface profile
z	coordinate normal to and away from heating surface (defined in Fig. 3)
z_1	coordinate normal to and towards heating surface (defined in Fig. 3)

Superscripts

*	non-dimensional

Greek symbols

χ	parameter defined in Eq. (12)
δ	vapor layer thickness (defined in Fig. 3)
ε	emissivity
κ	curvature
μ	viscosity
ϕ	angle defined in Fig. 3
ρ	density
σ	surface tension
σ_{sb}	Stefan-Boltzmann constant

Subscripts

exp	experiment (measured)
f	liquid
g	vapor
low	lower surface
max	maximum
min	minimum
neck	droplet neck region
patch	droplet patching point
pred	predicted
sat	saturation
up	upper surface
w	wall (heating surface)

Among the many mechanisms important to spray cooling, LFP represents a crucial transition point having appreciable impact on cooling performance in quenching operations, as will be discussed in the next subsection. LFP is also important to macro- and micro-channel flow boiling and jet impingement, in that it can be encountered during post-CHF operation, as the heating surface becomes solely dependent on the cooling provided by individual droplets [7–10].

The present study aims to address the most elemental phenomenon for the LFP, that of an individual sessile droplet. It is the opinion of the present authors that successful modeling of sessile droplet LFP will serve as a rational starting point before tackling more complex situations, such as LFP for individual impinging droplets and sprays. In fact, those more complex situations represent important future research targets for the present authors.

1.2. Importance of Leidenfrost point

Over the past three to four decades, processing of metal alloy parts with superior mechanical properties has demanded significant improvement to industrial heat treatment practices. Heat treatment is a three-stage process [11]: (a) *solution heat treating* (preheating) to high temperature (for a sufficient time) to allow alloying elements to dissolve uniformly within the primary metal grains, forming a solid solution, (b) *quenching* to near room temperature, during which time the solid solution is ideally kept intact, becoming a supersaturated solution, and (c) *age-hardening*, reheating the part to an intermediate temperature (for an optimal duration), allowing hardening compounds to nucleate and then spread uniformly within the primary metal grains, resulting in desired microstructure. It is this optimal formation and dispersion of hardening compounds that imparts high strength and hardness to the alloy part. But, for the heat treatment to be successful, it is vital that quenching proceed as rapidly as possible, otherwise the hardening compounds would precipitate prematurely along the boundaries rather than within the primary metal grains, resulting in a microstructure that cannot be enhanced during the subsequent age-hardening, therefore compromising mechanical properties of the part produced.

Two common quenching methods are *bath quenching* and *spray quenching* [11]. Comparatively speaking, bath quenching is slow, therefore posing the afore-mentioned risk of compromising microstructure. Additionally, bath quenching is problematic when heat treating complex-shaped alloy parts, especially those having both thick and thin sections, since, in the absence of spatial control of the cooling process, thin sections would cool faster than thick, which may result in large spatial variations in both microstructure

and mechanical properties, let alone risk of warping thin sections. On the other hand, spray quenching offers two key advantages over bath quenching: (a) faster cooling rate and (b) ability to tackle spatial variations of cooling rate for complex-shaped parts. Faster cooling rate with sprays is achieved by breaking the liquid into fine droplets having large surface area to volume ratio, and which impinge upon the hot surface at high speed. And, spatial control is possible with the use of multiple, differently configured sprays to cool different parts of the alloy part. Here, thick (large thermal mass) sections would be targeted by dense sprays, and thin (small thermal mass) sections by light, such that the entire part would cool rapidly but also uniformly.

From a heat transfer standpoint, quenching an alloy part from very high temperature to room temperature involves a succession of heat transfer regimes: *film boiling*, *transition boiling*, *nucleate boiling*, and *single-phase liquid cooling*, each exhibiting unique heat transfer characteristics [6,12]. These regimes are easily identifiable with the aid of the *boiling curve* (commonly used with heat-flux-controlled cooling applications) and the *quench curve*. Because of vast of differences in dominant heat transfer mechanisms between regimes, quenching proceeds at drastically different rates when traversing these regimes. This notion is clearly reflected in the quenching curve, Fig. 1(a), shown here for simplicity using the example of bath quenching. First, film boiling is dominated by formation of a vapor layer along the entire hot surface. Because of very low thermal conductivity of vapor, cooling rate in film boiling is quite slow. Within the transition boiling regime, liquid contact ensues with portions of the surface (while other portions continue to endure film boiling), which causes appreciable improvement in heat transfer and therefore faster cooling rate. The nucleate boiling regime is marked by abundance of vapor bubbles nucleating, growing, and departing from the surface at high frequency, thereby providing the best heat transfer, and therefore fastest cooling rate, of all four regimes. With further decreases in surface temperature, nucleation ultimately subsides as the quench enters the single-phase regime, becoming solely dependent on heat transfer to single-phase liquid, which is reflected by appreciable slowing of cooling rate.

The vast changes in cooling rate between the four regimes points to the importance of transition points between successive regimes: (a) *Leidenfrost point (LFP)*, separating film and transition boiling, (b) *critical heat flux (CHF)*, separating transition and nucleate boiling, and (c) *onset of single-phase liquid cooling* (also referred to as *onset of boiling* in situations involving increasing rather than decreasing surface temperature). For heat treating operations, LFP is arguably the most important parameter governing cooling rate during the quench. This notion can be explained as follows. First, to accelerate the quench rate, it is important that the alloy exit the slow film boiling regime (*i.e.,* reach LFP) as early as possible. Second, the detrimental growth of hardening compounds along the boundaries of primary metal grains occurs around the LFP temperature range. In fact, the other two transition points of the quench curve are far less consequential, given the limited impact of cooling rate on microstructure at their respective temperature ranges. These facts point to the paramount importance of LFP and need to (a) uncover its underlying mechanism(s), (b) determine parametric influences that dictate its occurrence, and, perhaps most crucially, (c) develop a predictive model.

1.3. Leidenfrost point for sessile droplets

Having discussed the importance of LFP, the current subsection will address the complexity of LFP prediction. Clearly, there are major differences between LFP for bath quenching (as depicted in Fig. 1(a)) and spray quenching, as LFP for the latter occurs within impinging droplets rather than a liquid pool. As pointed out earlier,

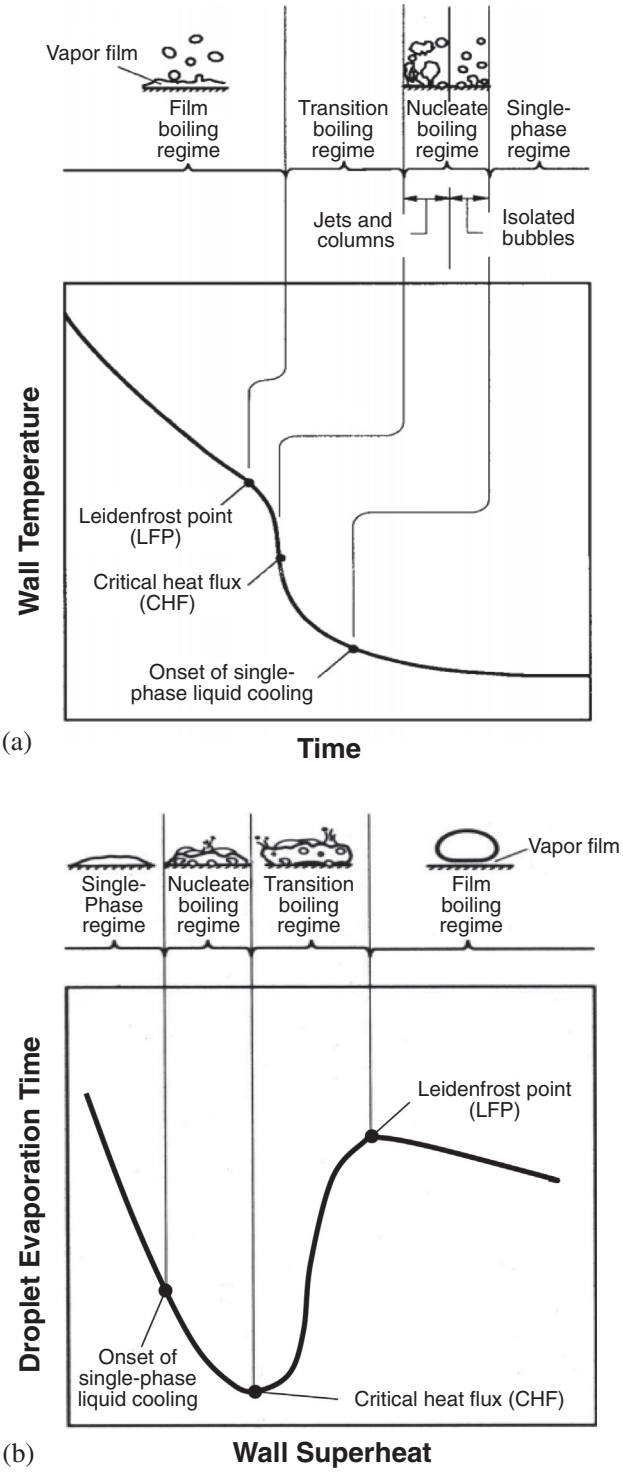

Fig. 1. (a) Bath quenching curve. (b) Evaporation time curve for a sessile droplet.

it is the primary goal of the present study to address the most elemental foundation for LFP in individual droplets. By focusing on an individual sessile droplet, it will be possible to construct a theoretical model for this important phenomenon, which can be modified in future studies to address added effects of droplet inertia on LFP for impinging droplets and sprays.

Generally speaking, LFP for a sessile droplet can be identified using thermodynamic or hydrodynamic perspectives [12]. With the former, LFP corresponds to the longest droplet evaporation

time in the high-temperature range, Fig. 1(b), while the latter focuses on the disruption of the vapor layer between the droplet and the wall (illustrated in top schematics in Fig. 1(b)). In either case, wall temperatures higher than the LFP (within the film boiling regime) result in a continuous vapor film forming between the droplet and the wall, while temperatures below the LFP (within transition boiling regime) trigger partial collapse of the vapor film and direct contact of liquid with the wall, which is accompanied by vastly improved heat transfer performance and therefore faster cooling rate.

1.4. Experimental studies on LFP

Review of literature reveals that work to date on the LFP has been overwhelmingly experimental, which may be explained by the difficulties in characterizing liquid-vapor-solid interfacial features. In most cases, the LFP is experimentally determined by plotting droplet evaporation time against wall temperature as shown in Fig. 1(b). A large portion of the sessile droplet literature has been focused on identifying LFP on polished surfaces rather addressing the important role of surface roughness. Examples of measured sessile droplet LFP temperatures for different surface roughness conditions [13–17] are provided in Table 1. The tabulated temperatures show considerable variations in LFP for a given fluid resulting from effects of such parameters as ambient pressure, wall material, wettability, impurities, *etc*. Furthermore, there are contradictory or indeterminate findings regarding effects of liquid subcooling, initial droplet size and method of droplet deposition [16]. Overall, clearly characterized LFP data are quite sparse, and therefore careful additional work is needed in the future to amass a comprehensive database spanning many fluids as well as broad ranges of relevant parameters in which surface topography is carefully characterized. Nonetheless, despite differences in measured LFP values between studies, an overall trend is clearly evident from Table 1: *LFP temperature increases with increasing surface roughness*.

1.5. Predictive tools for LFP

Although considerable experimental LFP databases have been reported in prior literature for different fluids, wall materials and surface roughness, only a small subset of these studies yielded convincing capture of the underlying physical mechanism responsible for initiating the LFP, which is an essential starting point for constructing any predictive model.

Of the few studies that did yield mechanistic depictions and models for sessile droplet LFP, vastly different physical descriptions were proposed, including *hydrodynamic instability* [18], *thermomechanical effect* [19], *wettability effect* [20], and both *homogeneous and heterogeneous nucleation* [21,22]. These works are summarized in Table 3 of Ref. [16], in which assessment of prior model predictions showed considerable inaccuracies in predicting LFP temperature. Furthermore, it is noteworthy that most models were developed for perfectly smooth surfaces, as no information concerning surface roughness effects was reported, which brings into doubt the ability of the same models to tackle practical surfaces.

In one successful effort to account for surface roughness, Bernardin and Mudawar [23] measured LFP based on carefully characterized surface cavities, and proposed a sessile droplet LFP model that was structured around cavity activation and bubble growth, *i.e.,* approaching LFP initiation from the transition boiling regime rather than from film boiling. Their model was developed for relatively smooth surfaces with roughness on the same magnitude as cavity radii (0.1–1.0 μm). The model showed good agreement with experimental data for the small roughness levels considered, and provided a lower limit for LFP temperature on rougher surfaces.

Table 1
Examples of previous experimental studies including surface roughness effects on sessile droplet LFP.

Reference	Fluid	Wall material	Surface condition	Measured LFP Temp. (°C)
Baumeister *et al.* [17]	water	pyrex glass	R_q = 0.0762–0.1016 μm	515, >700
		stainless steel		305, 325
		brass		230, 235
		brass (fresh polish)		>200
		gold (fresh polish)		<184
		aluminum		230, 235
		aluminum (fresh polish)		155, >200
		aluminum	R_q = 0.635 μm	265
	ethanol	pyrex glass	R_q = 0.0762–0.1016 μm	260, 360
		stainless steel		190
		aluminum		155, 157
		aluminum (fresh polish)		157
Bernardin & Mudawar [16]	FC-72	aluminum (polished, particle blasted, rough sanded)	R_a = 0.097 μm	90
			R_a = 0.97 μm	110
			R_a = 2.96 μm	120
	acetone		R_a = 0.097 μm	135
			R_a = 0.97 μm	155
			R_a = 2.96 μm	160
	benzene		R_a = 0.097 μm	175
			R_a = 0.97 μm	220
			R_a = 2.96 μm	218
	water		R_a = 0.097 μm	171
			R_a = 0.97 μm	250
			R_a = 2.96 μm	263
Kruse *et al.* [15]	water	stainless steel (modified with laser pulse)	R_q = 4.4 μm	316
			R_q = 5.7 μm	340
			R_q = 4.5 μm	360
			R_q = 6.0 μm	405
			R_q = 5.4 μm	455
Hassebrook *et al.* [14]	water	steel (modified with laser pulse)	R_q = 4.8 μm	425, 460, 525
			R_z = 24.9 μm	
Misyura [13]	water	aluminum	R_q = 0.04–0.07 μm	158
			R_q = 3–6 μm	185

1.6. Objectives of present study

The main goal of the present study is to provide a clear mechanistic depiction of sessile droplet LFP, which is used to construct a predictive theoretical model for this phenomenon capable of capturing LFP trends for practical surfaces. As discussed in the next section, the model development will be based on predicting the temporal behavior of the vapor film beneath the droplet during the droplet shrinkage following deposition on the hot wall.

The model presented here represents a first elemental step towards future understanding of the more complex problems of an individual impacting droplet or spray. It should be mentioned the proposed model concerns practical rough flat surfaces, rather than surfaces with artificial (nano or micro) pillars or pores. The reader should consider Ref. [24] for information concerning the enhancement of the LFP using artificial surface features.

2. Mathematical formulation

2.1. Proposed physical mechanism

As depicted in Fig. 2, the model presented here captures temporal shrinkage of the sessile droplet following deposition upon the heating surface, as well as associated changes in vapor layer (especially thickness) as the LFP is approached from the high-temperature (film boiling) side. It will be shown below that, as the vapor layer thickness gradually decreases, the droplet approaches the surface, eventually beginning to be penetrated by surface roughness protrusions, which causes the insulating vapor layer to collapse and film boiling to cease.

2.2. Model assumptions

As mentioned in the previous subsection, the droplet will be levitated by its own vapor when contacting a very high temperature surface. The droplet shape as well as thickness of the vapor layer beneath the droplet vary with droplet volume (*i.e.,* with time). As shown in Fig. 2, an initially deposited large droplet tends to spread laterally under gravity and can be modeled in cylindrical coordinates with a height of approximately double the capillary length [25]. While, on the other extreme, if the initial droplet is small, or following gradual evaporation of an initially large droplet, the droplet becomes more and more spherical.

This hypothesis points to the importance of predicting instantaneous size and shape of the evaporation droplet and especially temporal behavior of the vapor layer. Several important assumptions are adopted in the model development:

(1) Upper surface of the droplet is exposed to constant ambient pressure.
(2) Initial subcooling of the droplet shortly following deposition is ignored (most experimental studies do not report information on initial subcooling).
(3) Any internal circulation within the liquid droplet is neglected.
(4) Any temperature variations within the droplet during the evaporation process are ignored, *i.e.,* the droplet is assumed to maintain constant saturation temperature, T_{sat}, throughout the evaporation transient.
(5) The wall is assumed to possess sufficiently high thermal mass that its temperature, T_w, remains unchanged during the evaporation transient.
(6) The vapor layer is very thin compared to the droplet size (actually, it is typically one to two orders of magnitude smaller than the droplet diameter).

2.3. Vapor flow dynamics

When the surface temperature exceeds the LFP temperature, a thin vapor layer is generated between the droplet and heating surface, which prevents the droplet from direct contact with the wall. Since the LFP is postulated to occur when thickness of the vapor layer decreases to a sufficiently low level that the droplet begins to be penetrated by elevated surface features, accurate determination of the layer thickness is indispensable for the LFP model development. Equally important is the ability to determine shape of the liquid-vapor interface beneath the droplet. Fig. 3 is used to define key nomenclature used in the model development.

Because of very small thickness of the vapor layer, the momentum equation for the vapor flow is given by

$$\frac{dP_g}{dr} = \mu_g \frac{\partial^2 u}{\partial z^2}\,, \tag{1}$$

where P_g, μ_g, and u are local vapor pressure, vapor viscosity, and local radial vapor velocity, respectively.

Radial vapor velocities at the bottom surface of the droplet are expected to be small and may be neglected. And, at the solid surface, non-slip boundary condition means a zero radial velocity. Therefore, the radial velocity is subject to the following boundary conditions:

$$u(z=0) = 0 \tag{2a}$$

$$\text{and } u(z=\delta) = 0\,. \tag{2b}$$

Integrating Eq. (1) subject to the above boundary conditions yields the following expression:

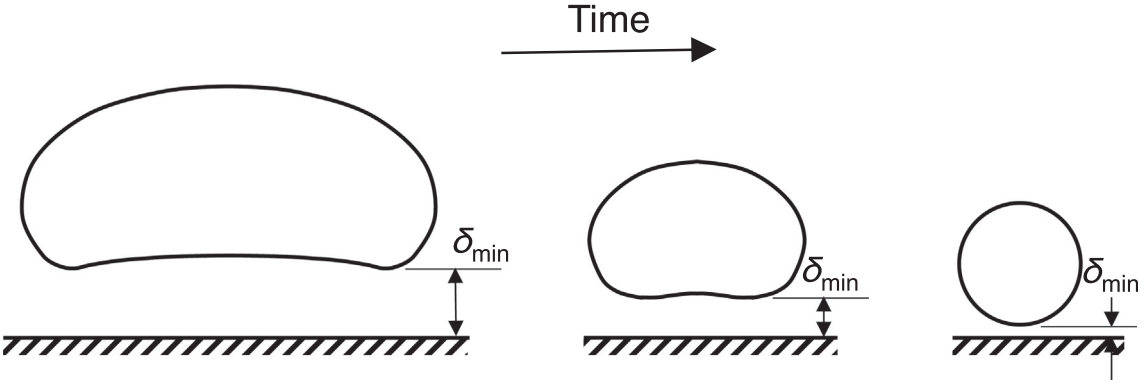

Fig. 2. Temporal variations of droplet size and shape in the film boiling regime.

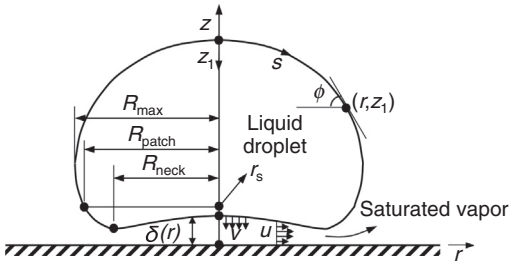

Cylindrical coordinate system r-z_1 for droplet's upper surface shape
Cylindrical coordinate system r-z for droplet's lower surface shape
Spherical coordinate system r_s for mass diffusion

Fig. 3. Schematic diagram of a sessile droplet levitated by a vapor layer on the heating surface.

$$u(r,z) = \frac{1}{2\mu_g}\frac{dP_g}{dr}\left(z^2 - \delta z\right). \tag{3}$$

Pressure in the vapor layer is found from a force balance normal to the droplet surface [26,27],

$$P_g = P_0 - \left(\rho_f g\delta + \sigma\kappa\right), \tag{4}$$

where P_0 is the liquid pressure, and ρ_f, g, σ and κ are liquid density, gravity, surface tension, and surface curvature, respectively.

Vapor velocity w in the z-direction is obtained by using the continuity equation,

$$\frac{1}{r}\frac{\partial(ru)}{\partial r} + \frac{\partial w}{\partial z} = 0. \tag{5}$$

With the boundary condition $w = 0$ at $z = 0$, Eq. (5) can be integrated to yield

$$w = -\frac{1}{r}\frac{\partial}{\partial r}\left[r\frac{dP_g}{dr}\frac{z^2}{12\mu_g}(2z - 3\delta)\right], \tag{6}$$

which, combined with Eq. (4), reduces to the form

$$w = \frac{1}{r}\frac{d}{dr}\left[\frac{z^2}{12\mu_g}(2z - 3\delta)\, r\frac{d}{dr}\left(\rho_f g\delta + \sigma\kappa\right)\right]. \tag{7}$$

The vapor production rate per unit area, v (having units of velocity), from the lower droplet interface can be obtained from the heat balance

$$\rho_g v h_{fg} = \frac{k_g}{\delta}\left(T_w - T_{sat}\right) + \varepsilon\sigma_{sb}\left(T_w^4 - T_{sat}^4\right), \tag{8}$$

h_{fg}, k_g, ε and σ_{sb} being the latent heat of vaporization, vapor conductivity, emissivity and Stefan-Boltzmann constant, respectively. In the present study, vapor density ρ_g is calculated using the Peng-Robinson equation of state [28]. In a previous study [29], both surface topography and temperature were found to influence the spectral emissivity. To simplify the model calculations, total emissivity in Eq. (8) is assumed constant. Table 2 provides emissivity values used for different surface materials and roughness [30].

Some of the previous studies on film evaporation of a sessile droplet [31–33] proposed that radiation effect is negligible, therefore vapor production rate is dictated entirely by conduction across the vapor layer; they also proposed that evaporation from the top surface of the droplet may be neglected. However, the present authors opted to consider effects of additional evaporation due to both radiation to the bottom surface of the droplet and mass diffusion from the top surface. While radiation is shown to account for only 5–8% (as discussed below) of the total evaporation, mass diffusion from the top surface is quite significant. Without accounting for radiation and top surface evaporation, calculated droplet diameter was larger than measured values, especially during the later stages of the evaporation period corresponding to very small droplet size. Therefore, the radiation heat transfer term in Eq. (8) is retained in the development of the present LFP model.

Table 2
Emissivity values for different surface materials and roughness [30].

Surface material	Temperature (K)	Emissivity
Aluminum:		
Highly polished	500–850	0.039–0.057
Commercial sheet	373	0.09
Heavily oxidized	422–778	0.20–0.31
Brass:		
Highly polished	520–650	0.028–0.037
Copper:	390	0.023
Polished	373	0.052
Heavily oxidized	298	0.78
Glass:		
Smooth	295	0.94
Pyrex	533–811	0.85–0.95
Gold:		
Highly polished	500–900	0.018–0.035
Nickel:		
Polished	373	0.072
Oxidized	922–1528	0.59–0.86
Platinum:		
Polished	500–900	0.054–0.104
Stainless steel:		
Polished	373	0.074

Mass conservation for z-direction vapor velocity w requires that

$$w|_{z=\delta} = -v \tag{9}$$

By substituting Eqs. (8) and (9) into (7), and introducing capillary length

$$l = \left(\sigma/\rho_f g\right)^{1/2}, \tag{10}$$

the following equation is obtained for dimensionless vapor layer thickness:

$$\frac{d}{dr^*}\left[r^*\delta^{*3}\frac{d}{dr^*}\left(\kappa^* + \delta^*\right)\right] - \frac{12\chi r^*}{\delta^*} = 0, \tag{11}$$

where parameters with an asterisk are nondimensionalized using capillary length, with $r^* = r/l$, $\delta^* = \delta/l$, and $\kappa^* = \kappa l$, and parameter χ is a dimensionless parameter accounting for fluid properties and surface heating,

$$\chi = \frac{\mu_g\left[k_g(T_w - T_{sat}) + \varepsilon\sigma_{sb}\, l\,\delta^*\left(T_w^4 - T_{sat}^4\right)\right]}{\rho_g\sigma\, l\, h_{fg}}. \tag{12}$$

2.4. Droplet shape analysis

As illustrated in Fig. 2, the shape of a sessile droplet that is suspended above the heating surface by a vapor layer depends largely on the initial droplet volume and surface temperature. Therefore, it is vitally important to determine the accurate shape of the sessile droplet when modeling the LFP. As shown in Fig. 3, the droplet surface can be divided into two parts that are 'separated' by a locus of patching points along the perimeter of a circle of radius R_{patch}. It should be noted that as the droplet shrinks by evaporation to small spherical size, the neck region, indicated by R_{neck} in Fig. 3, will no longer exist.

2.4.1. Upper droplet surface

From the perspective of mechanical equilibrium, shape of the upper surface of the sessile droplet is governed by a balance between hydrostatic pressure and capillary pressure [27],

$$\sigma\kappa - \rho_f g z_1 = \sigma\kappa_0, \tag{13}$$

where κ_0 is surface curvature at $r = 0$ and z_1 is measured for now from the droplet apex. By introducing capillary length, Eq. (13) can be nondimensionalized to the form

$$\kappa^* = z_1^* + \kappa_0^*. \tag{14}$$

It is convenient to solve Eq. (14) in terms of arc length s along the surface from the droplet apex, as shown in Fig. 3. Introducing angle ϕ between the tangent of the arc length and the horizontal line, Eq. (14) can be transformed into

$$\frac{d\phi}{ds^*} = z_1^* + \kappa_0^*, \tag{15a}$$

$$\frac{dr^*}{ds^*} = \cos\phi, \tag{15b}$$

$$\text{and} \quad \frac{dz_1^*}{ds^*} = \sin\phi. \tag{15c}$$

subject to the boundary conditions

$$\phi(0) = 0, \tag{16a}$$

$$r^*(0) = 0, \tag{16b}$$

$$\text{and} \quad z_1^*(0) = 0, \tag{16c}$$

all length parameters being nondimensionalized relative to capillary length.

The three ordinary differential Eqs. (15a)–(15c) can be easily solved by the fourth-order Runge-Kutta method from the droplet apex to the patching point. Several prior studies indicated that an accurate position of the patching point has a negligible effect on the droplet shape [26,27]; this observation was also verified in the present calculation.

2.4.2. Lower droplet surface

The curvature for the lower surface of the droplet is approximated as [26,34]

$$\kappa^* = \frac{\frac{d^2\delta^*}{dr^{*2}} + \frac{1}{r^*}\left[1 + \left(\frac{d\delta^*}{dr^*}\right)^2\right]\frac{d\delta^*}{dr^*}}{\left[1 + \left(\frac{d\delta^*}{dr^*}\right)^2\right]^{3/2}}, \tag{17}$$

where δ^* is the nondimensional vapor layer thickness beneath the sessile droplet obtained from Eq. (11).

Introduce the two variables f_1 and f_2, defined as

$$\frac{d\delta^*}{dr^*} = f_1 \tag{18a}$$

$$\text{and} \quad \frac{d\kappa^*}{dr^*} = f_2, \tag{18b}$$

Eqs. (17) and (11) can be rearranged, respectively, into the two following ordinary differential equations,

$$\frac{df_1}{dr^*} = \kappa^*\left(1 + f_1^2\right)^{3/2} - \frac{1}{r^*} f_1\left(1 + f_1^2\right) \tag{19}$$

$$\text{and} \quad \frac{df_2}{dr^*} = \frac{1}{r^*\delta^{*3}}\left[\frac{12\chi r^*}{\delta^*} - (f_1 + f_2)\frac{d(r^*\delta^{*3})}{dr^*}\right] - \frac{df_1}{dr^*}. \tag{20}$$

To ensure a continuous droplet shape, the solution of the lower surface must match that of the upper at the patching point. In other words, the position, slope, and curvature at the patching point must be continuous. Therefore, the boundary conditions for Eqs. (17)–(20) should be as follows: (1) $f_1 = f_2 = 0$ at $r = 0$ (due to zero slope and zero curvature resulting from symmetry), and (2) at $r = R_{patch}$, f_1 and κ must match corresponding values obtained from the upper surface equations.

Eqs. (17)–(20) along with these boundary conditions constitute a typical boundary-value problem, and can be solved by combining the Runge-Kutta and shooting methods. The strategy here is to start from conditions at $r = R_{patch}$ with arbitrarily assumed $\delta(R_{patch})$ and $f_2(R_{patch})$, which are iterated during calculation until a satisfactory solution is found that satisfies the condition $f_1(0) = f_2(0) = 0$.

2.5. Droplet evaporation rate

As indicated in Ref. [35], evaporation from the upper surface of the droplet cannot be ignored, even for large droplets. In the present model, surface evaporation is accounted for over the entire surface of the droplet. The evaporation is the sum of two parts, one from the lower surface, resulting from heat conduction and radiation, and the other from the top surface, governed by mass diffusion.

For the lower surface, the evaporation rate is given by

$$\frac{dm_{low}}{dt} = -\int \rho_g v dA_{low} \tag{21}$$

where v is the vapor production rate per unit area (defined in Eq. (8)) and A_{low} the lower surface area of the droplet, which can be obtained through integration.

By introducing the definition of capillary length l from Eq. (10), Eq. (21) is used to develop the following dimensionless equation for the time rate of change of droplet volume, V_{low}, resulting from evaporation from the lower surface:

$$\frac{dV_{low}^*}{dt} = -\left[\frac{k_g(T_w - T_{sat})}{\rho_f h_{fg} l^2}\int \frac{dA_{low}^*}{\delta^*} + \frac{\varepsilon\sigma_{sb}\left(T_w^4 - T_{sat}^4\right)}{\rho_l h_{fg} l}\int dA_{low}^*\right], \tag{22}$$

where $V^*_{low} = V_{low}/l^3$, $A^*_{low} = A_{low}/l^2$, and $\delta^* = \delta/l$.

For the upper surface, the steady-state diffusion equation is used (assuming quasi-steady behavior during the droplet shrinkage),

$$\frac{1}{r_s^2}\frac{d}{dr_s}\left(r_s^2\frac{dc}{dr_s}\right) = 0, \tag{23}$$

where r_s is the spherical coordinate measured from the center of circle constituting locus of the patching points, which is different from the cylindrical coordinate r used in the droplet shape and vapor layer analysis. The spherical coordinate system is introduced here to make it more convenient to describe the local mass flux perpendicular to the upper surface element. Eq. (23) is subject to the following boundary conditions [36]:

$$c|_{r_s = R_s} = \frac{MP}{T_{sat} R_g} \tag{24a}$$

$$\text{and} \lim_{r_s \to \infty} c = 0, \tag{24b}$$

where c, M, and R_g are, respectively, vapor concentration in air (in kg/m^3), molar mass of vapor, and vapor gas constant, and R_s is distance from the origin of the spherical coordinates to the droplet surface. With boundary conditions (24a) and (24b), Eq. (23) can be solved to yield

$$c = \left(\frac{MP}{T_{sat} R_g}\right)\frac{R_s}{r_s}. \tag{25}$$

The mass flux (in kg/m^2/s) along the upper surface is then

$$\dot{m} = -D\frac{dc}{dr_s}\bigg|_{r_s=R_s} = \frac{DMP}{R_s T_{sat} R_g}, \tag{26}$$

where D is the mass diffusion coefficient, which is calculated using Wilke and Lee's method [37].

The time rate of change of droplet mass resulting from evaporation from the upper surface is expressed as

$$\frac{dm_{up}}{dt} = -\int \dot{m} dA_{up}. \tag{27}$$

Introducing Eq. (26) and definition of capillary length l from Eq. (10) into Eq. (27) yields the following dimensionless relation for time rate of change of droplet volume, V_{up}, resulting from evaporation from the upper surface:

$$\frac{dV^*_{up}}{dt} = -\frac{DMP}{T_{sat} R_g \rho_l l^2}\int \frac{dA^*_{up}}{R^*}, \tag{28}$$

where $V^*_{up} = V_{up}/l^3$, $A^*_{up} = A_{up}/l^2$, and $R^* = R/l$.

Finally, the time rate of change of droplet volume resulting from evaporation from the entire surface can be expressed as the sum of rates from the bottom surface, Eq. (22), and top surface, Eq. (28),

$$\frac{dV^*}{dt} = \frac{dV^*_{up}}{dt} + \frac{dV^*_{low}}{dt}. \tag{29}$$

3. Calculation procedure

In executing the various model calculations, all liquid properties and vapor mass diffusion coefficient are evaluated at saturation temperature, while all vapor layer properties are calculated at the mean of wall and saturation temperatures. Since the accuracy of computation depends on size of time step used, especially for small droplets, time step dependence tests are conducted for each case to ensure calculation accuracy.

The main calculation procedure is as follows:

(1) Eqs. (15a)–(15c) are used to determine upper surface shape, *i.e.*, to calculate, respectively, three unknown parameters of angle, ϕ, dimensionless radial distance, r^*, and dimensionless vertical distance, $z_1{}^*$ using the fourth-order Runge-Kutta method from the droplet apex to the patching point.
(2) Value of dimensionless curvature κ^* at the patching point is then obtained using Eq. (14), then $\kappa^*(R_{patch})$ and $r^*(R_{patch})$ values are introduced into the boundary conditions for Eqs. (17)–(20).
(3) Using a combination of Runge-Kutta and shooting methods, dimensionless vapor layer thickness, δ^*, curvature of the lower surface, κ^*, as well as their first derivatives, are determined using Eqs. (17)–(20), respectively.
(4) Time rate of change of dimensionless droplet volume is calculated by substituting calculated thermophysical properties and droplet shape parameters results back into Eqs. (22), (28) and (29), and initial droplet volume for the next time step is obtained.
(5) Repeat Steps (1–4) until the droplet evaporation completes.

It is worth noting that, other than wall temperature and saturation temperature, the additional input variable in the droplet shape analysis is curvature $\kappa_0{}^*$ at the droplet apex (Eqs. (13)–(20); which is the only independent variable). However, the main parameter here is droplet volume, which can be calculated only after the entire droplet shape is determined for a given κ_0^*. In the present study, the droplet is treated as a rotator by spinning the surface curve around the z-axis, and the droplet volume is obtained by integration. For each wall temperature condition, several values of $\kappa_0{}^*$ are chosen in advance to calculate the droplet shape then volume so as to obtain a piecewise polynomial curve fit between V^* and $\kappa_0{}^*$. This enables the determination of $\kappa_0{}^*$ for a given droplet volume.

4. Results and discussion

4.1. Verification of model predictions

4.1.1. Comparison of droplet radius results

To validate the present model, predictions of droplet size evolution are first compared with experimental data available from the literature, experimental conditions for which are summarized in Table 3. As shown in Fig. 4, calculated temporal records of *equivalent* droplet diameter D (=$2(A_F/\pi)^{0.5}$, where A_F is calculated frontal area of the droplet) or mass are in close agreement with measured values for different liquids, initial droplet sizes, and wall temperatures [33,38–40], which supports the accuracy of the predictive approach used. The data used here were selected based on availability of all parameters required for model execution.

4.1.2. Comparison of vapor layer thickness results

Fig. 5 shows fairly good agreement between minimum thickness of the vapor layer beneath the droplet, calculated using the present model and liquid nitrogen data of Chandra and Aziz [33]. The data in this plot correspond to the film boiling regime before any droplet-surface contact takes effect. Also shown are predictions of a previous model by Gottfried *et al.* [36], which was based on the assumption of a flat droplet underside, *i.e.,* spatially constant vapor layer thickness. Better predictions by the present model compared to the previous constant thickness model provide validity support to the assumptions adopted here.

Biance *et al.* [41] provided an alternative model assuming a flat liquid-vapor interface for large droplets with radius larger than the capillary length. Since the Chandra and Aziz experiments involved initial droplet radii smaller than the capillary length, the predictions of Biance *et al.* were not included in Fig. 5.

4.2. LFP model predictions and analysis

It is important to note that thus far comparisons of model predictions with experimental data for droplet diameter (and mass), Fig. 4, and vapor layer thickness, Fig. 5, concern a film boiling droplet, *i.e.,* one not contacting the wall. The primary goal of the present paper is to provide a predictive method for the LFP, taking into account effects of surface roughness for practical surfaces.

The fundamental premise of the proposed LFP model is as follows. For relatively high surface temperatures corresponding to the film boiling regime, a sessile droplet will be separated from the surface by a continuous vapor layer. Fig. 6 shows predicted droplet shape evolution and vapor layer development at different times for a water droplet with an initial diameter of $D_0 = 2$ mm and surface temperature of 600 K. Notice how vapor layer thickness decreases as the droplet shrinks in size with time, which is consistent with findings from recent direct numerical simulations of sessile droplet evaporation [42]. A similar trend of decreasing vapor layer thickness is predicted for a given droplet diameter as wall temperature is decreased (this will be shown in the subsequent section). Therefore, decreasing droplet size and/or decreasing wall temperature serve to decrease the vapor layer thickness, causing the droplet underside to approach the surface. Eventually, the vapor layer becomes so thin that it begins to be penetrated by surface roughness protrusions, which causes the insulating vapor layer to partially collapse due to sudden liquid contact with the wall. This mechanism essentially defines the onset of the LFP as

Table 3
Experimental droplet evaporation data from the literature used to validate present model.

Reference	Fluid	Surface material	Initial size	Wall temperature
Gottfried *et al.* [40]	ethanol	polished stainless steel	V_0 = 13.91 μL	492 K
Avedisian & Fatehi [39]	water	polished stainless steel	D_0 = 3.04 mm	565 K
			D_0 = 2.98 mm	620 K
			D_0 = 2.96 mm	680 K
	heptane	polished stainless steel	D_0 = 2.73 mm	565 K
			D_0 = 2.47 mm	620 K
			D_0 = 2.90 mm	680 K
	decane	polished stainless steel	D_0 = 2.82 mm	620 K
Chandra & Aziz [33]	liquid nitrogen	glass/polished copper	V_0 = 4.2 μL	290 K
Nakoryakov *et al.* [38]	water	copper	m_0 = 0.1 mg	483 K

well as points to the importance of surface roughness as a key parameter influencing LFP. Overall, it will be shown below that, aside from fluid and pressure surrounding the droplet, the LFP is dictated by effects of three key parameters: (1) droplet size, (2) surface temperature, and (3) surface roughness.

4.2.1. Surface characterization

To better illustrate the influence of surface roughness on the LFP, it is useful to briefly explain roughness characterization for practical surfaces. Surface roughness is important for many modes of heat transfer including not only convection but radiation as well [43,44]. Fig. 7 shows an example of a surface profile comprised of variations of surface height y_i over a sampling length L. Also shown are important statistical surface parameters [45]: arithmetic mean roughness, R_a, root mean square roughness, R_q, and average peak-to-valley height of surface features, R_z. Notice that it is R_z that is important to LFP prediction since it provides a physical measure of surface protrusion through the vapor layer. As indicated in Fig. 7, it is hypothesized operating conditions culminating in vapor layer thickness (actually minimum thickness because of spatial variations of the vapor layer) greater than R_z will prevent penetration of surface protrusions into the droplet, therefore resulting in film boiling. The LFP will occur when the minimum vapor layer thickness decreases to the magnitude of R_z, such that protrusions just begin to penetrate the droplet.

Unfortunately, R_z values are not always available from experimental sessile droplet studies. However, values of R_a are commonly reported. Also available in some studies is the root mean square roughness, R_q.

In the absence of R_z values from prior experiment studies on sessile droplet LFP, the present authors opted to determine the relationship between R_z, R_q and R_a using roughness profiles measured by the authors for four different materials (brass, copper, stainless steel and aluminum) using Talysurf PGI 840 surface contact profilometer from Taylor Hobson. The samples were initially washed with distilled water and then dried with a clean cloth. Different roughness levels were imparted to the surfaces by sanding with different grades of emery paper in a counterclockwise circumferential direction. The profilometer featured a very fine (2 μm) stylus that traversed the surface to record the roughness values over the sampling length.

A subset of these measurements is shown in Fig. 8. Individual profiles show that the surface roughness distribution is stochastic and, as to be expected, the values of R_z and R_a for each surface are considerably different from one another. Fig. 9(a) shows a correlation for R_z with R_a based on 30 data points measured in the present study along with 525 additional data points from 54 sources (those are related to surface analysis and not to heat transfer). This correlation is used in all subsequent calculations presented in this paper when comparing model predictions to LFP data from previous experimental studies reporting surface characteristic based on R_a. Similarly, Fig. 9(b) shows the correlation of R_q to R_a based on 458 data points from 23 sources. By combining this correlation with the R_z to R_a correlation from Fig. 9(a), it is also possible to compare model predictions to LFP data from previous studies reporting surface characteristic based on R_q.

It is worth noting that a profilometer was used for almost all the surface roughness measurements in the literature. As demonstrated in Fig. 3 of Ref. [23], physical size of the diamond stylus may limit the accuracy of measured profiles, since very fine surface features cannot be detected. This resolution limit, as well as error in the correlations provided in Fig. 9(a) and (b) will undoubtedly impact uncertainty of LFP predictions. A more accurate method to determine R_z from R_a or R_q is currently unavailable and calls for further comprehensive and systematic study.

4.2.2. LFP model assessment

When discussing surface roughness effects, time evolution of droplet size and vapor layer thickness for a water droplet at different wall temperatures is provided as example. Fig. 10(a) shows, for a water droplet with initial diameter of 4.0 mm, temporal variations of equivalent droplet radius (half of equivalent droplet diameter, D) and minimum vapor layer thickness, δ_{min} (see definition in Fig. 2) for three surface temperatures. Notice how, for each surface temperature, δ_{min} decreases at first, reaching a minimum value, Min [δ_{min}], before increasing again in the final stage of evaporation as the droplet becomes too light to balance the upward pressure force generated by evaporation; a trend observed in a prior experimental study [46]. Fig. 10(a) shows that Min [δ_{min}] decreases monotonically with decreasing temperature, meaning the closest circumference of the droplet underside moves closer to the surface. This increases the likelihood of droplet penetration by surface protrusions and occurrence of the LFP condition. This temperature trend is consistent with experimental evidence of the LFP occurring when, starting in the film boiling regime, the surface temperature is gradually decreased. In terms of roughness effects, a key premise of the present model is that a rougher surface be able to penetrate a larger Min [δ_{min}], therefore at a higher temperature than a smoother surface. This trend, too, is consistent with experimental evidence.

The increase in LFP temperature on rougher surfaces could not be explained by previous models or correlations since they rarely addressed the influence of surface roughness. In other words, predictions based on prior predictive tools showed no differences in LFP temperature on surfaces with different roughness. On the contrary, the present model clearly points to the droplet underside being breached by tall surface roughness features during the droplet evaporation. At very high surface temperatures corresponding to the fully developed film boiling regime, Fig. 10(a) showed the vapor layer thickness can be considerably larger than the surface roughness features, rendering effects of the latter negligible. But, as the surface temperature is gradually decreased, the vapor layer thickness decreases, eventually approaching the height of tall surface features and triggering the LFP event.

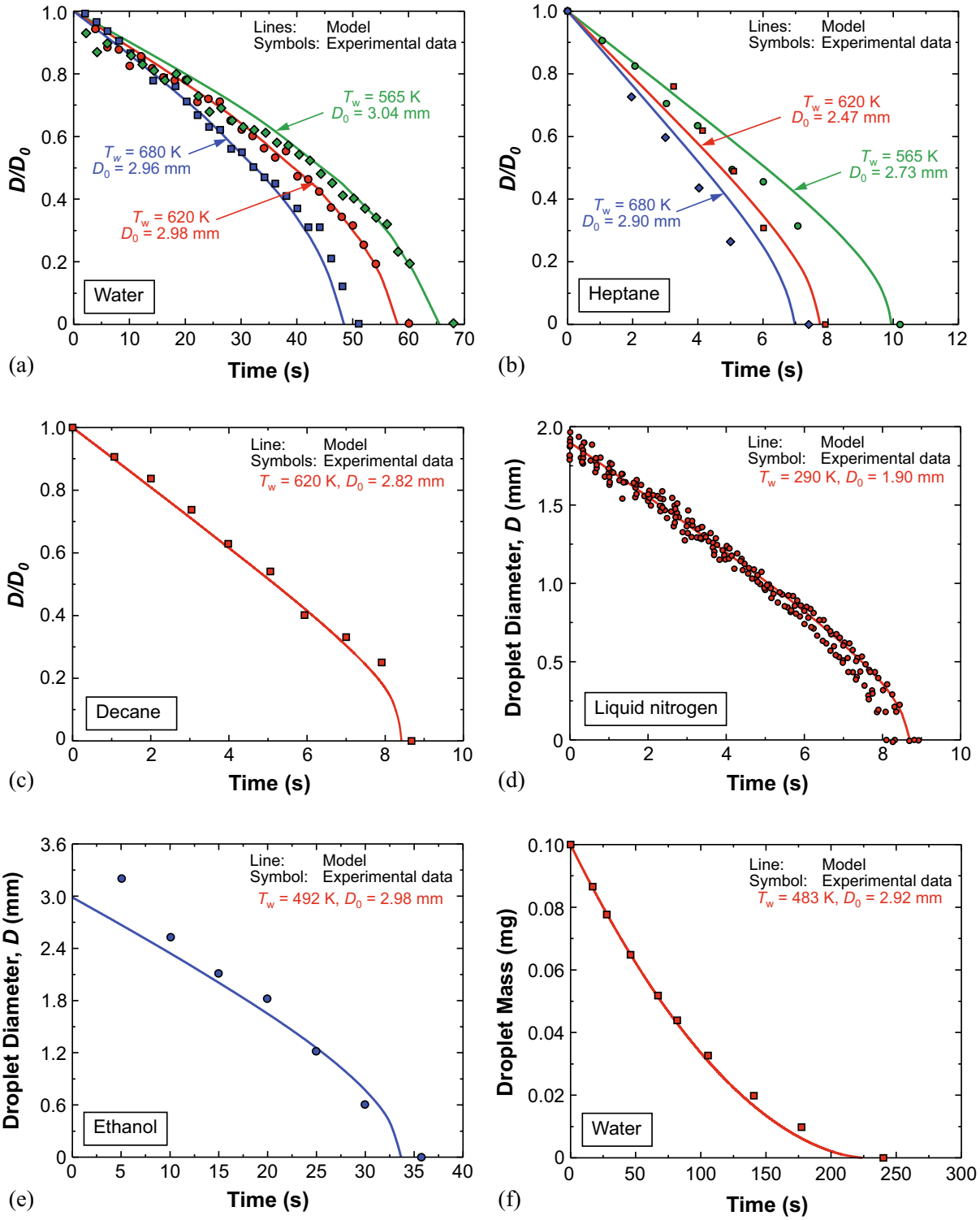

Fig. 4. Comparison of temporal results computed using present model versus dimensionless droplet diameter data of Avedisian and Fatehi [39] for (a) water, (b) heptane, and (c) decane; droplet diameter data of (d) Chandra and Aziz [33] for liquid nitrogen and (e) Gottfried et al. [40] for ethanol; and droplet mass data of Nakoryakov et al. [38]. All data in this figure correspond to the film boiling regime.

As mentioned earlier, contradictory inferences have been reported in prior studies concerning the effects of initial droplet size (D_0) on the LFP. This is clearly manifest in that some experimental results showed no dependence of LFP on D_0 [16,40], while others indicated LFP temperature increases with increasing D_0 [13,14]. The present model provides compelling reasons behind this discrepancy. Theoretically, when the tallest surface roughness features exceed the vapor layer thickness, liquid-solid contact will occur. But, despite the fact that surface roughness generally exhibits self-similarity, a larger droplet (which would also possess larger underside area) would provide greater spatial opportunity to contact tall surface features than a smaller droplet. Nonetheless, it is difficult to characterize droplet contact with tall surface features simply on a statistical basis.

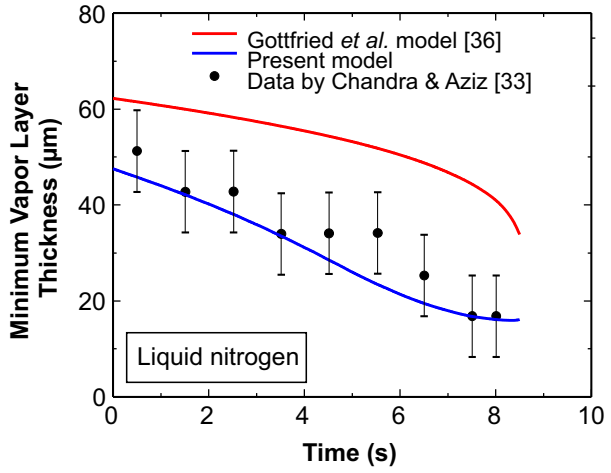

Fig. 5. Comparison of temporal variations of minimum thickness of vapor layer beneath a liquid nitrogen droplet measured by Chandra and Aziz [33] with predictions based on the present model and previous model by Gottfried et al. [36].

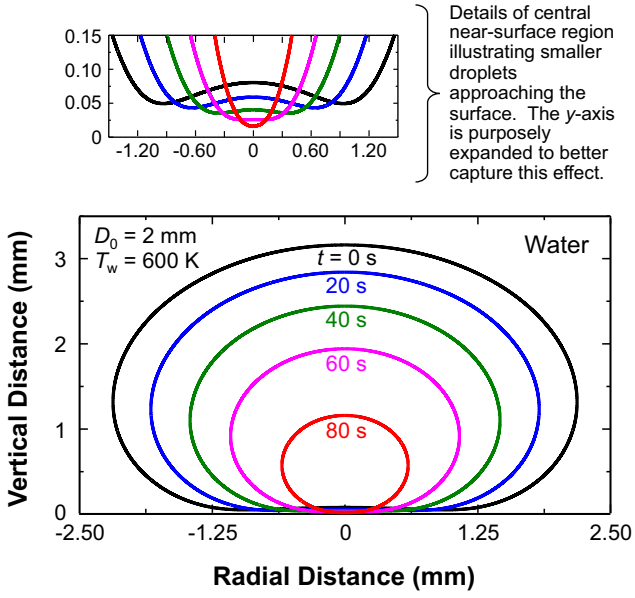

Fig. 6. Time evolution of droplet shape and vapor layer development for water droplet with $D_0 = 2$ mm and $T_w = 600$ K.

Instead, the present model provides a more systematic assessment of the roughness effects. The solid line in Fig. 10(b) shows, for the same water droplet considered in Fig. 10(a), with $D_0 = 4.0$ mm, the relationship between surface temperature and Min [δ_{min}]. For a surface with $R_a = 2.96$ μm and $R_z = 16.81$ μm, the *measured* LFP temperature is $T_w = 536$ K (263 °C). Notice that Min [δ_{min}] for this measured temperature corresponds to 72% of R_z as indicated by the arrows. Once a reasonable range is captured in terms of dependence on R_z, the model calculations are attempted at slightly higher and lower values, showing minor improvements within the range considered, with $0.75R_z$ yielding best predictions of experimental LFP data. Based on good overall agreement with the measured LFP temperature for different materials and surface roughness profiles, the value corresponding to 75% of R_z for each surface is used in the model.

To evaluate overall predictive accuracy of the present model, Fig. 11 shows predicted versus measured LFP temperatures, LFP_{pred} and LFP_{exp}, respectively, for three fluids. Overall accuracy of

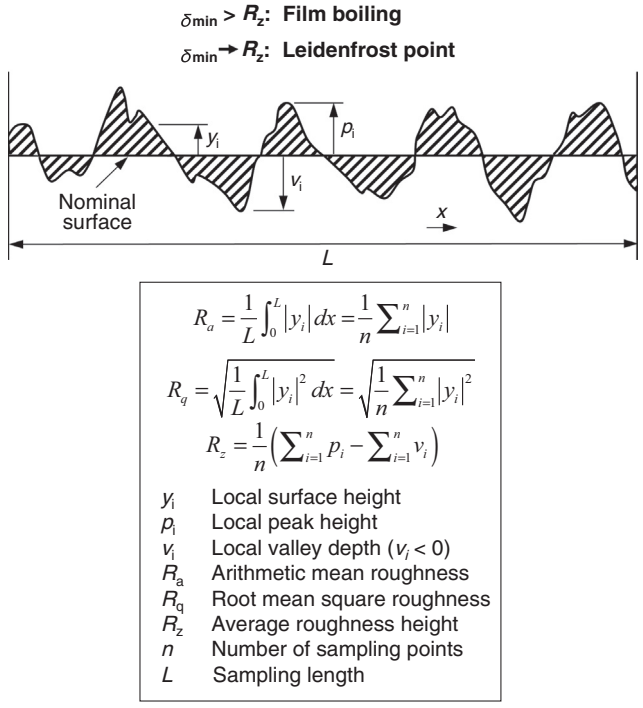

$$R_a = \frac{1}{L}\int_0^L |y_i|\,dx = \frac{1}{n}\sum_{i=1}^{n}|y_i|$$

$$R_q = \sqrt{\frac{1}{L}\int_0^L |y_i|^2\,dx} = \sqrt{\frac{1}{n}\sum_{i=1}^{n}|y_i|^2}$$

$$R_z = \frac{1}{n}\left(\sum_{i=1}^{n} p_i - \sum_{i=1}^{n} v_i\right)$$

y_i	Local surface height
p_i	Local peak height
v_i	Local valley depth ($v_i < 0$)
R_a	Arithmetic mean roughness
R_q	Root mean square roughness
R_z	Average roughness height
n	Number of sampling points
L	Sampling length

Fig. 7. Example of surface roughness profile, definition of key statistical parameters [45], and identification of criterion for the onset of Leidenfrost point.

predictions is assessed using the mean absolute error (MAE), which is defined as

$$\mathrm{MAE} = \frac{1}{n}\sum \frac{|\mathrm{LFP}_{exp} - \mathrm{LFP}_{pred}|}{\mathrm{LFP}_{exp}} \times 100\%, \quad (30)$$

where n is the total number of data points. The experimental data used here are carefully selected based on availability of all parameters needed to execute the model as well as surface roughness parameters.

With an MAE of 7.77%, the present LFP model shows good agreement with the available experimental data (especially for water cases). A primary attribute of the model is its highly analytical formulation, modified only by a single empirical parameter (Min [δ_{min}] = 0.75 R_z). Deviations between the predictions and data may be attributed to a couple of factors. First, as shown earlier in Fig. 9(a) and (b), there are deviations between measured and correlated R_z versus R_a and R_q versus R_a values, respectively. There may also be minor influences of solid wall thermal properties, which are not accounted for in the model.

4.2.3. Discussion on model limitations

The model developed in the current study constitutes a powerful analytical tool for predicting the LFP of a sessile droplet on practical surfaces, capable of accurately capturing detailed temporal variations of droplet size and vapor layer thickness as well as a trigger event for LFP.

However, attempts to apply the present formulation to a *very* highly polished surface with $R_a \sim 0.1$–1 μm were unsuccessful. Previous observations [47] reveal that when water and liquid hydrocarbons droplets become very small, levitation height of the droplet begins to fluctuate. This phenomenon might be attributed to natural convection of surrounding air (whose temperature is much lower than the surface temperature), where buoyancy-driven air currents with recirculating eddies can influence smaller droplets. In one study [46], small spherical Leidenfrost droplets below a certain critical size were observed to spontaneously

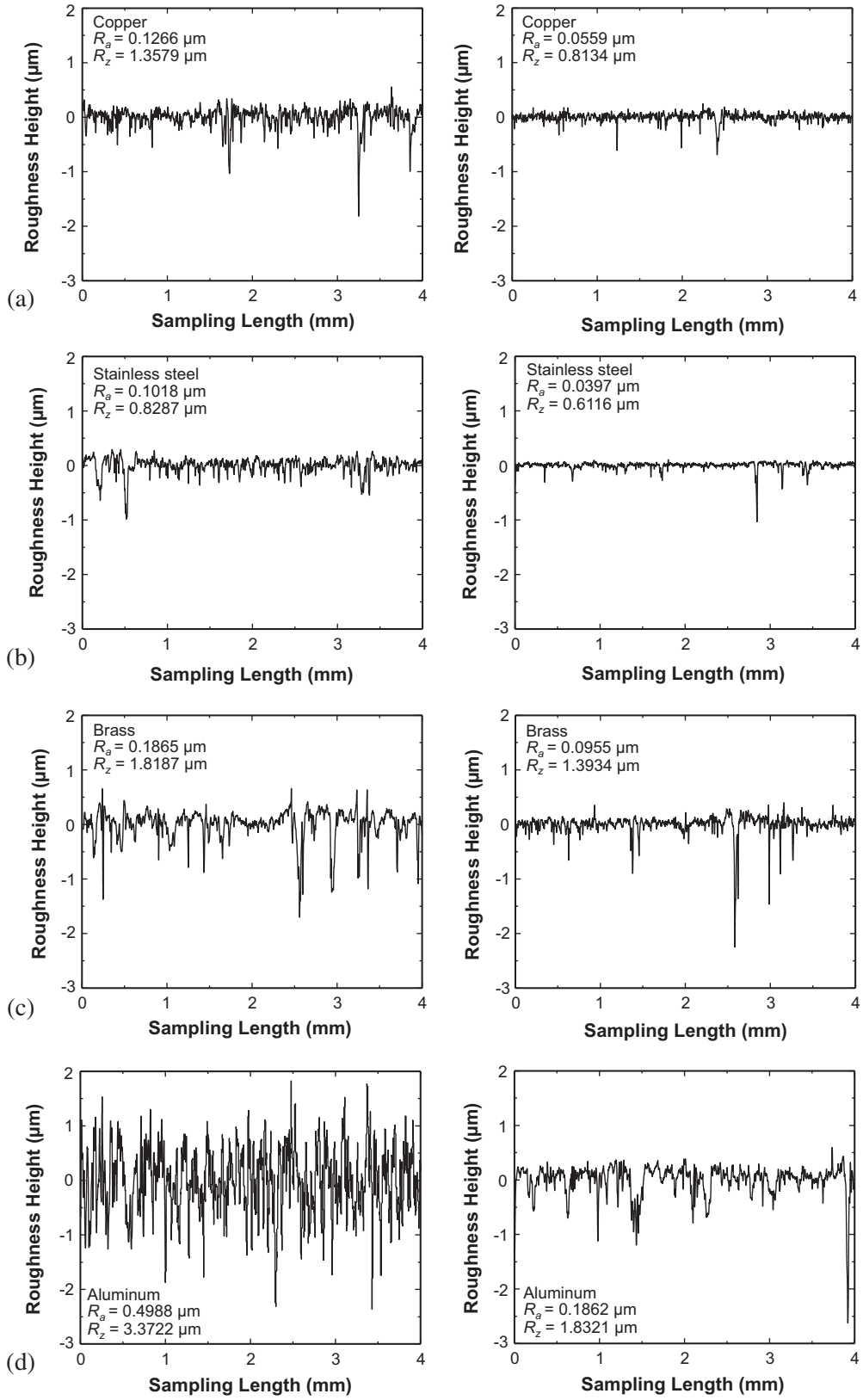

Fig. 8. Present surface profiles for (a) copper, (b) stainless steel, (c) brass, and (d) aluminum.

rebound from the hot surface. This is can be explained by noting trends in Fig. 10(a), where vapor layer thickness decreases to Min [δ_{min}] before increasing again during the last few seconds. For an extremely smooth surface, R_z is quite small, so is Min [δ_{min}]. Therefore, droplets will reach much smaller size than on a practical (rougher) surface, which would cause liquid-solid contact to occur at higher surface temperature than predicted by the present model.

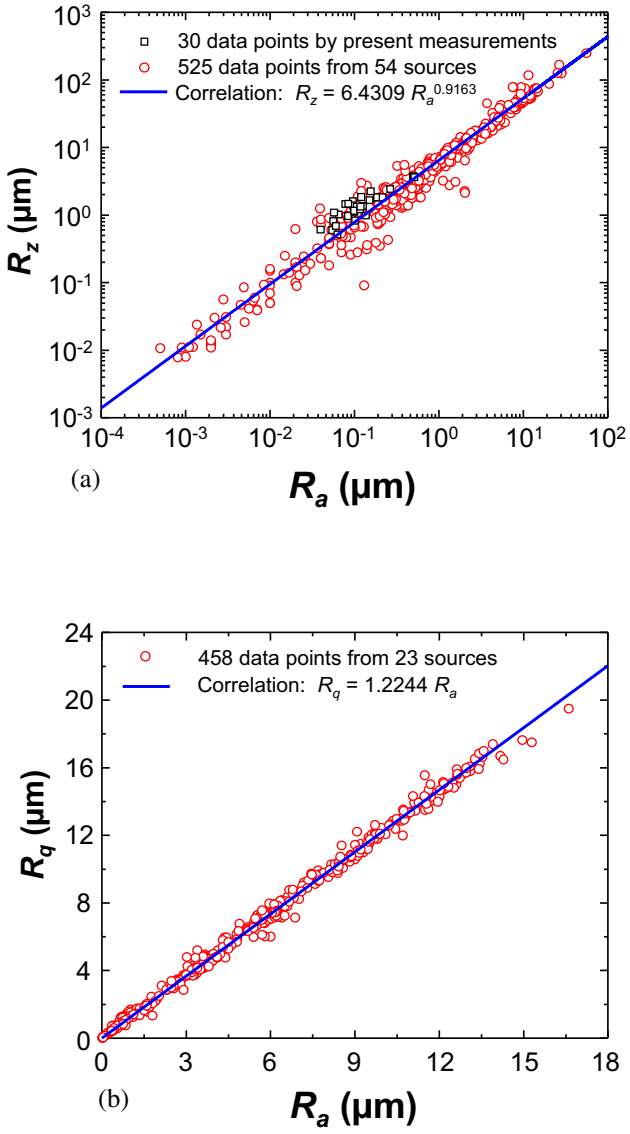

Fig. 9. (a) Correlation of R_z to R_a using present and previous surface profile data. (b) Correlation of R_q to R_a using previous surface profile data.

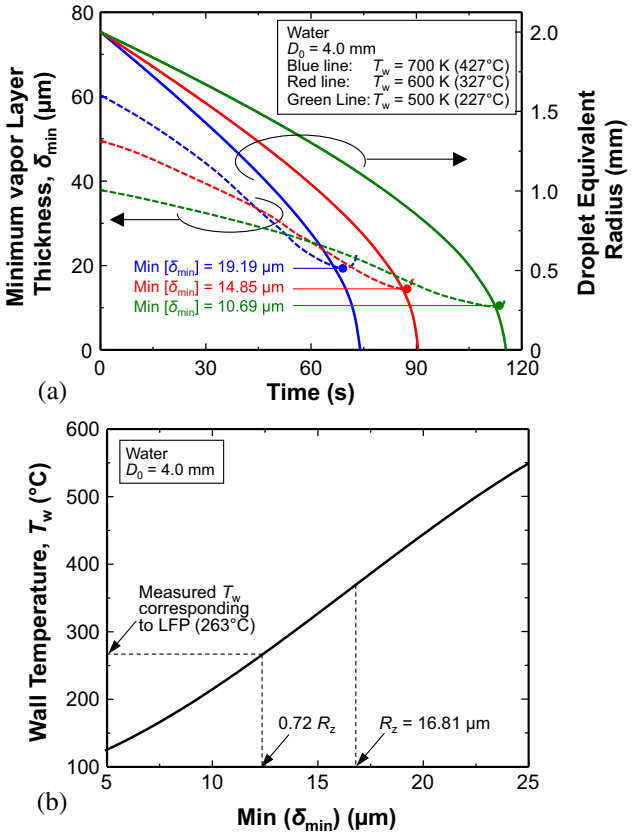

Fig. 10. (a) Time evolution of droplet size and minimum vapor layer thickness for a water droplet within the film boiling regime for different surface temperatures, and identification of Min [δ_{min}] for each temperature. (b) Variation of surface temperature with corresponding Min [δ_{min}].

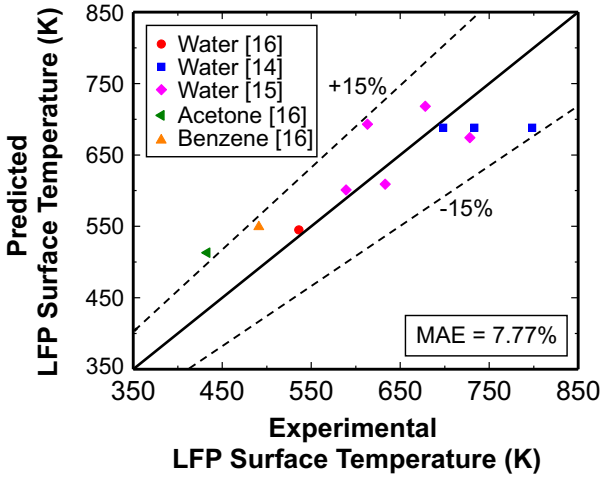

Fig. 11. Comparison of LFP surface temperature predicted by present model (corresponding to Min [δ_{min} = 0.75 R_z) with experimental data [14–16].

Another source of deviation between model predictions and measurements is rapid development of a very thin oxide layer on the metal surface during the initial preheating process. It is inevitable that microscopic (or even macroscopic) oxidation would roughen the surface, demanding a thicker Min [δ_{min}] and therefore higher LFP temperature.

It is also worth noting that, according to the experimental results of Bernardin and Mudawar [16], the effect of surface roughness on LFP temperature within the 'polished range' (obtained using different grades of diamond paste) is negligible. This points to a need for future work to address the unique nature of *very* highly polished surfaces when using the present model.

Despite the inability to predict LFP for highly polished surfaces, further validation of the LFP mechanism adopted in the model is provided in Fig. 12 even for such surfaces. In Ref. [48], a polished stainless-steel surface was used to measure the LFP temperature for different liquids, but no surface roughness parameters were provided. Using the present model, Min [δ_{min}] was calculated for the same surface using the *measured* LFP temperature. Fig. 12 shows calculated Min [δ_{min}] values are all within a well-defined range. This proves the LFP mechanism adopted in the model, that LFP is reached when a certain range of the surface protrusions penetrate the underside of the droplet. Overall, this constitutes indirect proof of the model assumptions even for highly polished surfaces.

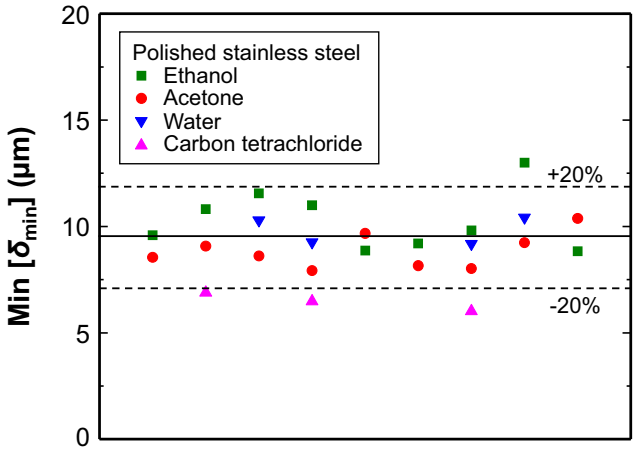

Fig. 12. Calculated Min [δ_{min}] for different liquids on a polished stainless steel surface using measured LFP temperatures [48].

5. Conclusions

This paper presented a theoretical model for the Leidenfrost phenomenon for a sessile droplet. The model is comprised of sub-models addressing temporal variations of droplet shape and vapor layer thickness separating the droplet from the heating wall, and evaporation from the droplet's upper and lower interfaces. It is shown that a minimum in the vapor layer thickness is achieved during the evaporation process; this is where the lower interface is closest to the heating surface. It is also shown that, starting from the film boiling regime (where the droplet is completely separated from the heating surface by the vapor layer), reducing surface temperature causes monotonic thinning of the vapor layer. The main premise (trigger event) of the model is that the Leidenfrost condition is achieved when surface temperature reaches a level (Leidenfrost temperature) where the vapor layer thickness minimum becomes sufficiently small to enable surface roughness protrusions to breach the droplet underside. This paper provided detailed assessment of all the sub-models, as well as showed the effectiveness of the model at predicting the Leidenfrost temperature for practical surfaces with known surface topography. Key conclusions from the study are as follows:

(1) Because of the highly stochastic nature of surface roughness, a statistical measure of surface height is essential to identifying conditions leading to a breach of the droplet underside and therefore initiation of the Leidenfrost phenomenon.
(2) The model shows good accuracy in predicting temporal records of droplet size and shape and vapor layer thickness for different liquids and surface temperatures. Combined with an appropriate statistical measure of surface height, the model shows very good accuracy in predicting the Leidenfrost temperature, evidenced by a mean absolute error of 7.77%.
(3) Limitations of the model are carefully addressed. They include limited accuracy of surface topography measurements, and inability to capture experimentally observed oscillations of very small droplets on highly polished surfaces.

Declaration of Competing Interest

The authors declared that there is no conflict of interest.

Acknowledgments

Financial support from National Key Research and Development Program of China (Grant No. 2017YFA0700300), National Natural Science Foundation of China (Grant No. 51961135105, 91641117), Open subject of the State Key Laboratory of Engines (Tianjin University) (Grant No. K2018-04) and China Scholarship Council (Grant No. 201806060070) is gratefully acknowledged.

Appendix A. Supplementary material

Supplementary data to this article can be found online at https://doi.org/10.1016/j.ijheatmasstransfer.2019.118802.

References

[1] C.R. Kharangate, I. Mudawar, Review of computational studies on boiling and condensation, Int. J. Heat Mass Transf. 108 (2017) 1164–1196.
[2] I. Mudawar, Recent advances in high-flux, two-phase thermal management, J. Therm. Sci. Eng. Appl. 5 (2013) 021012.
[3] I. Mudawar, T.M. Anderson, Parametric investigation into the effects of pressure, subcooling, surface augmentation and choice of coolant on pool boiling in the design of cooling systems for high-power-density electronic chips, J. Electron. Packag. 112 (1990) 375–382.
[4] M.E. Johns, I. Mudawar, An ultra-high power two-phase jet-impingement avionic clamshell module, J. Electron. Packag. 118 (1996) 264–270.
[5] W.P. Klinzing, J.C. Rozzi, I. Mudawar, Film and transition boiling correlations for quenching of hot surfaces with water sprays, J. Heat Treat. 9 (1992) 91–103.
[6] G. Liang, I. Mudawar, Review of spray cooling – Part 1: Single-phase and nucleate boiling regimes, and critical heat flux, Int. J. Heat Mass Transf. 115 (2017) 1174–1205.
[7] C.O. Gersey, I. Mudawar, Effects of heater length and orientation on the trigger mechanism for near-saturated flow boiling critical heat flux—I. Photographic study and statistical characterization of the near-wall interfacial features, Int. J. Heat Mass Transf. 38 (1995) 629–641.
[8] J.C. Sturgis, I. Mudawar, Critical heat flux in a long, rectangular channel subjected to one-sided heating—I. Flow visualization, Int. J. Heat Mass Transf. 42 (1999) 1835–1847.
[9] J.C. Sturgis, I. Mudawar, Critical heat flux in a long, rectangular channel subjected to one-sided heating—II. Analysis of critical heat flux data, Int. J. Heat Mass Transf. 42 (1999) 1849–1862.
[10] J. Lee, I. Mudawar, Critical heat flux for subcooled flow boiling in micro-channel heat sinks, Int. J. Heat Mass Transf. 52 (2009) 3341–3352.
[11] G. Liang, I. Mudawar, Review of spray cooling–Part 2: High temperature boiling regimes and quenching applications, Int. J. Heat Mass Transf. 115 (2017) 1206–1222.
[12] G. Liang, I. Mudawar, Review of drop impact on heated walls, Int. J. Heat Mass Transf. 106 (2017) 103–126.
[13] S.Y. Misyura, The effect of Weber number, droplet sizes and wall roughness on crisis of droplet boiling, Exp. Therm Fluid Sci. 84 (2017) 190–198.
[14] A. Hassebrook, C. Kruse, C. Wilson, T. Anderson, C. Zuhlke, D. Alexander, G. Gogos, S. Ndao, Effects of droplet diameter and fluid properties on the Leidenfrost temperature of polished and micro/nanostructured surfaces, J. Heat Transf. 138 (2016) 051501.
[15] C. Kruse, T. Anderson, C. Wilson, C. Zuhlke, D. Alexander, G. Gogos, S. Ndao, Extraordinary shifts of the Leidenfrost temperature from multiscale micro/nanostructured surfaces, Langmuir 29 (2013) 9798–9806.
[16] J.D. Bernardin, I. Mudawar, The Leidenfrost point: experimental study and assessment of existing models, J. Heat Transf. 121 (1999) 894–903.
[17] K.J. Baumeister, R.E. Henry, F.F. Simon, Role of the surface in the measurement of the Leidenfrost temperature, in: Augmentation of Convective Heat and Mass Transfer of the American Society of Mechanical Engineers Winter Annual Meeting, American Society of Mechanical Engineers New York, 1970, pp. 91–101.
[18] P.J. Berenson, Film boiling heat transfer from a horizontal surface, J. Heat Transf. 83 (1961) 351–358.
[19] D. Schroeder-Richter, G. Bartsch, Leidenfrost phenomenon caused by a thermo-mechanical effect of transition boiling. A revisited problem of non-equilibrium thermodynamics, in: Fundamentals of Phase Change: Boiling and Condensation, ASME-HTD, New York, 1990, pp. 13–20.
[20] A. Segev, S.G. Bankoff, The role of adsorption in determining the minimum film boiling temperature, Int. J. Heat Mass Transf. 23 (1980) 637–642.
[21] V.P. Carey, Liquid-vapor Phase-change Phenomena: An Introduction to the Thermophysics of Vaporization and Condensation Processes in Heat Transfer Equipment, second ed., Taylor and Francis, New York, New York, 2008.
[22] P. Spiegler, J. Hopenfeld, M. Silberberg, C.F. Bumpus, A. Norman, Onset of stable film boiling and the foam limit, Int. J. Heat Mass Transf. 6 (1963) 987–989.
[23] J.D. Bernardin, I. Mudawar, A cavity activation and bubble growth model of the Leidenfrost point, J. Heat Transf. 124 (2002) 864–874.
[24] M. Auliano, M. Fernandino, P. Zhang, C.A. Dorao, The Leidenfrost phenomenon on sub-micron tapered pillars, in: ASME 2017 15th International Conference

on Nanochannels, Microchannels, and Minichannels, Cambridge, Massachusetts, USA, 2017, pp. V001T008A003.
[25] D. Quéré, Leidenfrost dynamics, Ann. Rev. Fluid Mech. 45 (2013) 197–215.
[26] B. Sobac, A. Rednikov, S. Dorbolo, P. Colinet, Leidenfrost effect: accurate drop shape modeling and refined scaling laws, Phys. Rev. E 90 (2014) 053011.
[27] L. Duchemin, J.R. Lister, U. Lange, Static shapes of levitated viscous drops, J. Fluid Mech. 533 (2005) 161–170.
[28] J.S. Lopez-Echeverry, S. Reif-Acherman, E. Araujo-Lopez, Peng-Robinson equation of state: 40 years through cubics, Fluid Phase Equilib. 447 (2017) 39–71.
[29] C.-D. Wen, I. Mudawar, Modeling the effects of surface roughness on the emissivity of aluminum alloys, Int. J. Heat Mass Transf. 49 (2006) 4279–4289.
[30] J.P. Holman, Heat Transfer, tenth ed., The McGraw-Hill Companies, USA, New York, 2010, pp. 663–664.
[31] Y. Pomeau, M. Le Berre, F. Celestini, T. Frisch, The Leidenfrost effect: From quasi-spherical droplets to puddles, C.R. Mec. 340 (2012) 867–881.
[32] G. Bleiker, E. Specht, Film evaporation of drops of different shape above a horizontal plate, Int. J. Therm. Sci. 46 (2007) 835–841.
[33] S. Chandra, S.D. Aziz, Leidenfrost evaporation of liquid nitrogen droplets, J. Heat Transf. 116 (1994) 999–1006.
[34] J.H. Snoeijer, P. Brunet, J. Eggers, Maximum size of drops levitated by an air cushion, Phys. Rev. E 79 (2009) 036307.
[35] T.G. Myers, J.P.F. Charpin, A mathematical model of the Leidenfrost effect on an axisymmetric droplet, Phys. Fluids 21 (2009) 063101.
[36] B.S. Gottfried, K.J. Bell, Film boiling of spheroidal droplets. Leidenfrost phenomenon, Ind. Eng. Chem. Fundam. 5 (1966) 561–568.
[37] C.R. Wilke, C.Y. Lee, Estimation of diffusion coefficients for gases and vapors, Ind. Eng. Chem. 47 (1955) 1253–1257.
[38] V.E. Nakoryakov, S.Y. Misyura, S.L. Elistratov, Boiling crisis in droplets of ethanol water solution on the heating surface, J. Eng. Therm. 22 (2013) 1–6.
[39] C.T. Avedisian, M. Fatehi, An experimental study of the Leidenfrost evaporation characteristics of emulsified liquid droplets, Int. J. Heat Mass Transf. 31 (1988) 1587–1603.
[40] B.S. Gottfried, C.J. Lee, K.J. Bell, The Leidenfrost phenomenon: film boiling of liquid droplets on a flat plate, Int. J. Heat Mass Transf. 9 (1966) 1167–1188.
[41] A.L. Biance, C. Clanet, D. Quéré, Leidenfrost drops, Phys. Fluids 15 (2003) 1632–1637.
[42] Q. Guo, P. Cheng, Direct numerical simulations of sessile droplet evaporation on a heated horizontal surface surrounded by moist air, Int. J. Heat Mass Transf. 134 (2019) 828–841.
[43] C.-D. Wen, I. Mudawar, Emissivity characteristics of polished aluminum alloy surfaces and assessment of multispectral radiation thermometry (MRT) emissivity models, Int. J. Heat Mass Transf. 48 (2005) 1316–1329.
[44] C.-D. Wen, I. Mudawar, Emissivity characteristics of roughened aluminum alloy surfaces and assessment of multispectral radiation thermometry (MRT) emissivity models, Int. J. Heat Mass Transf. 47 (2004) 3591–3605.
[45] E.S. Gadelmawla, M.M. Koura, T.M.A. Maksoud, I.M. Elewa, H.H. Soliman, Roughness parameters, J. Mater. Process. Tech. 123 (2002) 133–145.
[46] F. Celestini, T. Frisch, Y. Pomeau, Take off of small Leidenfrost droplets, Phys. Rev. Lett. 109 (2012) 034501.
[47] S. Chandra, Droplet Evaporation and Combustion Near a Surface, Cornell University, Ithaca, NY, 1990.
[48] S. Nishio, M. Hirata, Direct contact phenomenon between a liquid droplet and high temperature solid surface, in: International Heat Transfer Conference 6, Begel House Inc., Toronto, Canada, 1978, pp. 245–250.